Nonlocal Near-Field Radiative Heat Transfer by Transdimensional Plasmonics

H. Salihoglu,[1] J. Shi,[1] Z. Li,[1] Z. Wang,[1] X. Luo,[1] I. V. Bondarev,[2] S.-A. Biehs,[3] and S. Shen[1,*]
[1]Department of Mechanical Engineering, Carnegie Mellon University, Pittsburgh, Pennsylvania 15213, USA
[2]Mathematics & Physics Department, North Carolina Central University, Durham, North Carolina 27707, USA
[3]Institut für Physik, Carl von Ossietzky Universität, 26111, Oldenburg, Germany

(Received 18 January 2023; accepted 25 July 2023; published 23 August 2023)

Using transdimensional plasmonic materials (TDPM) within the framework of fluctuational electrodynamics, we demonstrate nonlocality in dielectric response alters near-field heat transfer at gap sizes on the order of hundreds of nanometers. Our theoretical study reveals that, opposite to the local model prediction, propagating waves can transport energy through the TDPM. However, energy transport by polaritons at shorter separations is reduced due to the metallic response of TDPM stronger than that predicted by the local model. Our experiments conducted for a configuration with a silica sphere and a doped silicon plate coated with an ultrathin layer of platinum as the TDPM show good agreement with the nonlocal near-field radiation theory. Our experimental work in conjunction with the nonlocal theory has important implications in thermophotovoltaic energy conversion, thermal management applications with metal coatings, and quantum-optical structures.

DOI: 10.1103/PhysRevLett.131.086901

Near-field radiative heat transfer has attracted enormous interest for energy conversion [1,2], solid-state cooling [3,4], and thermal management [5,6] owing to the substantial radiation enhancement beyond Planck's law at nanoscale gaps. Dielectric response of materials essentially governs near-field thermal radiation due to its relationship with absorption (and emission based on Kirchoff's law). Based on fluctuational electrodynamics, near-field heat transfer theory generally relies on local dielectric properties and predicts continuously enhancing heat flux with a decreasing gap, d [3,7–12]. In the extreme nanometer-sized gaps ($d < 10$ nm), however, necessity of a nonlocal description arises to obtain nondivergent heat fluxes [13]. Thus, so far, theoretical attempts [14–17] to explain nonlocality have focused on the gap sizes in the extreme near field. Also, recent experimental studies [18–20] reveal inconclusive results for nonlocality. However, when considering thin plasmonic films there is another nonlocal effect which may alter the heat flux even at separation gaps of tens or hundreds of nanometers. Here, we provide an experimental proof of this nonlocality arising from plasmonic thin films with a thickness t of extreme nanometer-sized dimensions ($t < 10$ nm).

To control near-field thermal radiation, experimental studies [21–23] have so far mainly examined conventional bulk materials and thin films. Recent advancements in the fields of nanophotonics and plasmonics uncover that atomically thin plasmonic layers [24,25], also known as transdimensional plasmonic materials (TDPMs) [26], show unusual tunability in optical effects [27], and light-matter interactions [28]. In theory [29,30], out-of-plane confinement in an ultrathin metal film yields strong spatial dispersion and nonlocality [31–33] of dielectric response. While the thickness-dependent dielectric response due to the nonlocal effect provides a new degree of freedom for tunability [34–37], TDPMs are largely unexplored for controlling nanoscale thermal radiation.

Here, we examine both local and nonlocal dielectric responses of TDPMs within the framework of fluctuational electrodynamics. Based on a sensitive experimental platform capable of probing near-field signals as small as 0.1-1 nW at a gap of ~10 nm, we measure near-field radiative heat transfer between a silica sphere and a p-doped silicon substrate coated with an atomically thin layer of platinum (Pt) as TDPM, as shown in Fig. 1(a). Our experimental results show unprecedented dependence to nonlocal effects in the near-field heat flux at separations over a large range from tens of nanometers to micrometer gap sizes.

As shown in Fig. 1(a), we consider structure 1 as a bare planar semi-infinite medium (large sphere) and structure 2 as a multilayered planar structure consisting of a semi-infinite medium and a coated TDPM with a thickness t. Heat flux between the structures at temperatures T_1 and T_2 with a separation gap d is expressed by

$$q = \int_0^\infty \frac{d\omega}{2\pi}[\Theta(\omega, T_1) - \Theta(\omega, T_2)] \int_0^\infty \frac{d\kappa}{2\pi}\kappa\mathcal{T}(\omega, \kappa). \quad (1)$$

Here, $\Theta(\omega,T)$ is the mean energy of oscillators with frequency ω at temperature T and is expressed by $\hbar\omega/(e^{\hbar\omega/k_BT} - 1)$, where $\hbar$ and k_B represent the reduced Planck constant and the Boltzmann constant, respectively. κ denotes the wave vector component parallel to the planar

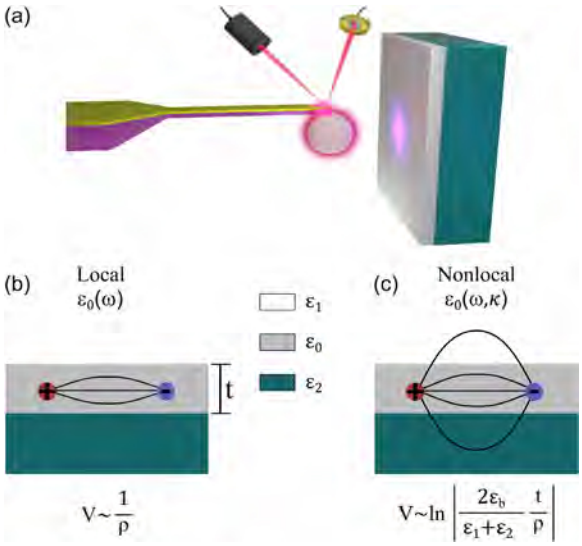

FIG. 1. (a) Schematic of the heat-exchanging structures (a large sphere medium, modeled as a plate for theoretical consideration, and a semi-infinite medium, dark teal, coated with an atomically thin metal film as the TDPM, light gray). Modeling of charge interactions based on the local (b) and nonlocal (c) approaches in a thin metal film ε_0, sandwiched between vacuum ε_1, and substrate ε_2. The local response assumes potential V is inversely proportional to the charge separations, $\sim 1/\rho$, as in a bulk whereas, based on the nonlocal model, $V \sim \ln|[2\varepsilon_b/(\varepsilon_1+\varepsilon_2)](t/\rho)|$. Here, ε_b denotes background response of the film.

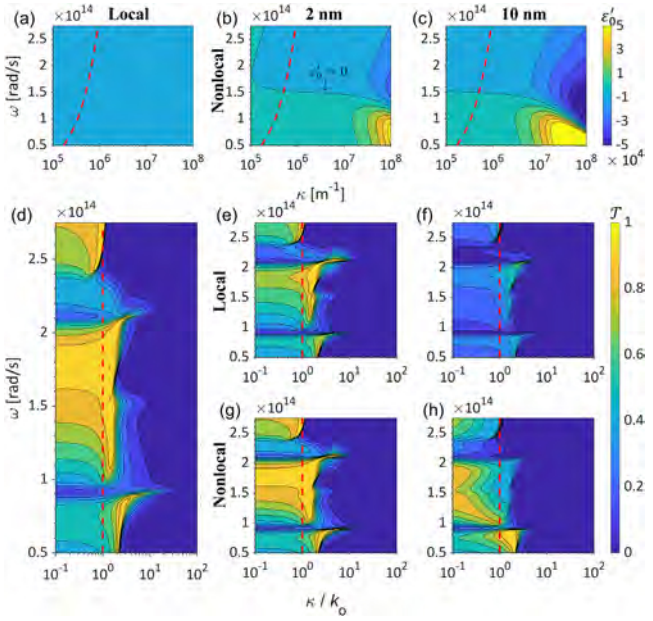

FIG. 2. Dielectric functions of Pt based on the local and nonlocal models. Real component of dielectric function ε_0' for Pt based on the local (a) $\varepsilon_0(\omega)$ and nonlocal (b)–(c) $\varepsilon_0(\omega,\kappa)$ model. The permittivity based on the nonlocal model exhibits strong κ-dependence for a thickness of 2 (b) and 10 (c) nm. In (b) and (c), contour lines are separated by 1×10^4 and the contour line at the very center of each panel corresponds to $\varepsilon_0'=0$, also pointed in (b). The color map scales ε_0'. Transmission probability, $\mathcal{T}(\omega,\kappa)$, across a 100-nm gap between a silica and a bare p-doped silicon (d), a silica and a p-doped silicon coated with a thin layer of Pt based on the local (e)–(f) and nonlocal (g)–(h) dielectric responses with respect to ω and κ/k_o.

surface. $\mathcal{T}(\omega,\kappa)$ represents the transmission probability of propagating $(\kappa < k_o = \omega/c)$ and evanescent $(\kappa > k_o)$ waves across the gap, and $\mathcal{T}(\omega,\kappa) \in [0,1]$. In the near field, the probability reads [38–40] (see Sec. 5 in [41] in the far-field)

$$\mathcal{T}(\omega,\kappa) = \frac{4\mathrm{Im}(r_1)\mathrm{Im}(r_2)}{|1-r_1r_2e^{2ik_zd}|^2}e^{-2\mathrm{Im}(k_z)d}. \tag{2}$$

Equation (2) shows that energy carried by the evanescent waves depends on reflection coefficient r_i with the imaginary component $\mathrm{Im}(r_i)$, for the planar structure i (see Sec. 4 in [41]) and the separation gap. These waves can be frustrated or surface waves. Energy of frustrated waves decays in proportion to $e^{-2\mathrm{Im}(k_z)d}$ and completely attenuates for $\mathrm{Im}(k_z) \gg (2d)^{-1}$. For surface waves, i.e., surface phonon and plasmon polaritons, the coupling of resonant waves between the interfaces across the gap, accounted by $|1-r_1r_2e^{2ik_zd}|^2$, compensates the exponential decay in a larger wave vector range so that $\mathcal{T}(\omega,\kappa)$ can have values even close to 1 for large κ.

Our understanding of dielectric response relies on local and nonlocal approaches. In this study, dielectric responses of both semi-infinite media are considered as local. Nonlocal response is only examined for TDPMs. The local model of TDPMs is derived based on the Drude model with classical equations of motion, where electromagnetic force acting on free electron clouds is uniform in the entire bulk medium [Fig. 1(b)]. Figure 2(a) shows the real component of the dielectric permittivity, ε_0', of a Pt ultrathin film based on the local model as a function of ω and κ (see the Supplemental Material [41] for local dielectric properties). Frequency dependent ε_0' varies from $\sim -1\times10^3$ at the high frequencies to $\sim -4\times10^3$ at the low frequencies. Figure 2(a) also reveals that the local response is independent of κ. Thus, dielectric response to a wave at a given frequency is independent of wave condition (propagating or evanescent in free space).

On the other hand, the quasiclassical approach [48] based on the Keldysh-Rytova (KR) potential suggests a nonlocal model, and differs from the Coulomb potential in that the out-of-plane confinement in an atomically thin film is considered when dielectric constants of substrate ε_1 and superstrate ε_2 surrounding the film, as shown in Fig. 1(c), are smaller than background dielectric response of the film, ε_b. Then, the Coulomb potential loses the out-of-plane dependence and becomes a purely in-plane 2D potential with the only remnant of the out-of-plane coordinate being the layer thickness to represent the size of the vertical confinement [Fig. 1(c)]. Consequently, Fourier transform

of the KR potential results in wave vector, κ, dependence. Applying the κ-dependent KR potential to the equation of motion of electrons returns a κ-dependent plasma frequency, resulting in a confinement-induced nonlocal Drude dielectric response. The KR potential varies with thickness due to change in the electrostatic interaction strength of electrons across the boundaries, and the plasma frequency of TDPMs becomes thickness dependent [27]. (see the Supplemental Material, Sec. 1 [41] for nonlocal dielectric properties).

To demonstrate the effect of nonlocality in dielectric function, we select a thin Pt film as the TDPM sandwiched between vacuum and a p-doped silicon substrate and plot real component ε_0' of the dielectric function in terms of ω and κ for thicknesses of 2 and 10 nm in Figs. 2(b) and 2(c), respectively (see Fig. S1 in [41] for the imaginary component). Based on the nonlocal model, dielectric responses exhibit both frequency and wave vector dependencies. The major frequency dependence arises from the comparable condition of ε_b, ε_1, and ε_2 at around $\omega \sim 1.5 \times 10^{14}$ where $\varepsilon_0' \sim 0$. The contour lines at the center, i.e., the line pointed in Fig. 2(b), represent $\varepsilon_0' = 0$ and divide Figs. 2(b) and 2(c) into two regions. Across the lines, ε_0' changes its sign from negative at the high frequencies to positive at the low frequencies, meaning that the optical response transitions from a metallic (metallic region) to dielectric response (dielectric region), respectively. Red dashed lines indicate the light line ($\kappa = k_o$). As κ varies from propagating ($\kappa < k_o$) to evanescent ($\kappa > k_o$) wave vectors for a given thickness, the strength of the response, related to absolute magnitude of the dielectric function, $|\varepsilon_0'|$, increases. We also recognize that with the increasing thickness, the strength of optical response increases for a given frequency and wave vector. Still, the responses for evanescent waves are stronger as compared to those of propagating waves. The comparison of Fig. 2(a) with Figs. 2(b) and 2(c) reveals that both the local and nonlocal models predict approximately the same strength of response for large wave vector ranges (evanescent waves). Conversely, for all thicknesses, dielectric response of atomically thin Pt over the wave vector range of propagating waves ($\kappa < k_o$) is weaker than that for bulk Pt.

Nonlocal and local transmission probabilities demonstrate strong contrast in energy transport capability of propagating and evanescent waves. Figures 2(d)–2(h) show the transmission probability as a function of ω and κ over both propagating and evanescent ranges for p-polarized waves at a separation gap of 100 nm between a silica plate and a p-doped silicon plate with and without Pt TDPM coating (see Fig. S7 in [41] for the transmission probability of s-polarized waves). We first consider the case without TDPM coating and plot the probability in Fig. 2(d). Within the evanescent wave vector range ($\kappa/k_o > 1$), modes with large wave vectors ($\kappa/k_o \sim 2$) excited at two narrow frequency bands around $\omega \sim 2 \times 10^{14}$ and $\omega \sim 1 \times 10^{14}$ rad s^{-1} carry most energy. These sharp peaks arise from SPhPs supported by silica and coupled across the separation gap. Also, frustrated waves ($\kappa/k_o \sim 1$) contribute to energy transport over a broad frequency range.

Now, we compare the transmission probabilities when a layer of Pt TDPM is considered on the silicon substrate. First, the transmission probabilities are plotted based on the local dielectric responses of TDPM with 2-, and 10-nm thicknesses in Figs. 2(e) and 2(f), respectively. From the comparison of Fig. 2(e) with Fig. 2(d), we point out that the presence of 2-nm-thick Pt diminishes the energy carried by propagating waves. Energy transport by SPhPs is mostly preserved. Increasing the film thickness to 10 nm almost prevents propagating and frustrated waves from contributing to energy transport. The local model predicts that, for propagating waves, optical response of a thin Pt layer is same with that of a perfect mirror, i.e., strong reflection (see Fig. S3 in [41] for plots of reflection coefficients of propagating waves). Similarly, the coupling strength of SPhPs weakens with the presence of 10-nm Pt. With the thickness, $\mathrm{Im}(r_2)$ (see Fig. S4 in [41]) approaches zero for the assembled structure, resulting in fast decaying $\mathcal{T}(\omega, \kappa)$.

The nonlocal transmission probability differs from the local one due to its wave condition (propagating or evanescent) dependence. We compare the bottom panels [Figs. 2(g) and 2(h)] with the top panels [Figs. 2(e)–2(f)] for a given thickness. Propagating waves carry a higher fraction of energy across the gap based on the nonlocal model because the nonlocal dielectric permittivity is weaker than that of the local permittivity in the corresponding wave vector range [see Figs. 2(a)–2(c)]. This indicates that based on the nonlocal response, the Pt film is more transparent to propagating waves and has minimal interference with energy transport capability of these waves across silica and silicon plates. In addition, we observe that the difference in energy transported by SPhPs (two major peaks) depends on the frequency ranges. The wave vector range of SPhPs at $\omega \sim 2 \times 10^{14}$ shrinks with a greater rate with thicker TDPM based on the nonlocal model because the strength of the metallic response gets stronger over broader wave vector range [see the metallic region in Figs. 2(b) and 2(c)] and exceeds that of the local model. In contrast, SPhPs at $\omega \sim 1 \times 10^{14}$ mainly preserve their energy transport capability compared to that of the local model. The reason is that the nonlocal TDPM film treats as a dielectric medium in the corresponding frequency and wave vector ranges [dielectric region as defined for Figs. 2(b) and 2(c)], and interferes less with the coupling of SPhP.

To examine the effect of nonlocality to near-field thermal radiation, we compute near-field heat transfer coefficient, $h \sim q/\Delta T$. Figure 3 shows the coefficient between silica and p-doped silicon coated with 2-, 5-, 10-, and 100-nm-thick TDPM films as a function of gap size. Both the local and nonlocal models estimate increasing heat transfer

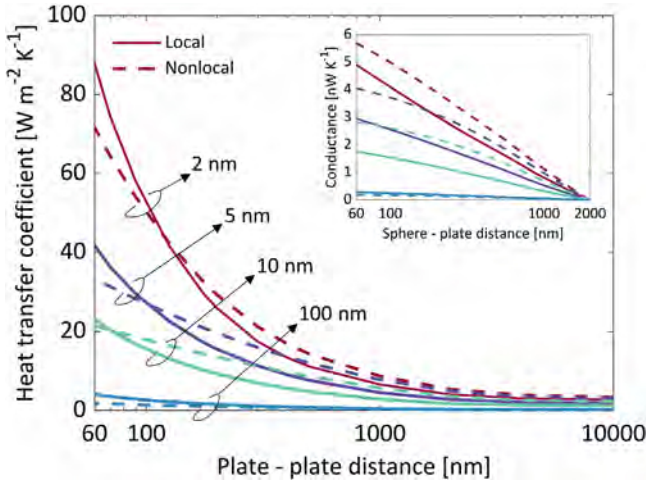

FIG. 3. Theoretical predictions of near-field radiation based on both the local and nonlocal models. Inset shows computed near-field conductance between the silica sphere and the silicon plate obtained using the Derjaguin approximation for the corresponding configurations. For later comparison with experiment, the numerical results are shifted such that the conductance is zero at a distance of 2 μm.

coefficient with respect to separation gap due to the evanescent wave contribution. The enhancement for a given separation gap decreases with the increase in film thickness based on both models. Comparison of nonlocal estimations with local ones indicates that the nonlocal near-field radiation predicts higher heat transfer for larger separation gaps because of the higher transmission probability for propagating and frustrated waves as discussed for Fig. 2. On the other hand, the nonlocal prediction is lower at separation gaps below a certain gap distance. This observation is consistent with the theoretical results in literature [49]. The lower heat flux arises because at shorter separations, waves with large κ values dominate the heat transfer and for the corresponding κ range, the corresponding dielectric response is even stronger than that of the local model. Thus, the coupling of polaritons between silica and p-doped silicon surfaces is weaker for large κ values. We also plot the theoretical near-field conductance between a silica sphere and a p-doped silicon plate based on the two models using the Derjaguin approximation. The inset of Fig. 3 reveals that the difference between the estimations of the two models is prominent for the sphere-plate configuration. We note that the nonlocal model is not only showing higher conductances than the local model as expected, but it also has the tendency of a small "saturation effect" for very small distances. The reason is that the heat flux for small gaps is smaller in the nonlocal model than in the local one as observed in Fig. 3.

To demonstrate the nonlocal effect from TDPMs, we conduct experiments for the near-field thermal radiation between a silica sphere and a p-doped silicon uncoated or coated with atomically thin Pt films of 2-, 5-, and 100-nm thickness. The schematic and the picture of our experimental platform are shown in Figs. 1(a) and 4(a), respectively. This platform was also employed in our previous work [50,51]. The inset and Fig. 4(b) show the real-time and the corresponding position-dependent deflection signal for the case with the uncoated substrate. The deflection signal monitors the near-field induced change (see Sec. 11 in [41] for details of the experiment). The Pt thin films are coated on the silicon substrates by sputtering. By lowering the plasma power, the deposition rate of Pt can be adjusted to be as low as ∼1 Å per second. We perform AFM measurements to characterize the roughness (see Sec. 7 in [41]) and find RMS roughnesses of ∼0.1, ∼0.2, and ∼0.4 nm for silicon without coating and with ∼2 and ∼5 nm coatings, respectively. The near-field measurements are carried out under a vacuum level of 1×10^{-6} Torr.

We plot experimental results of the near-field conductance measurements for the cases with the bare silicon plate and the silicon plates with atomically thin layers of ∼2, ∼5, and ∼100 nm in Fig. 4(c), showing that experimental results agree very well with the nonlocal near-field radiation predictions [see Fig. S9(b) in [41] for the estimation based on the local model and Figs. S10(a) and S10(b) in [41]

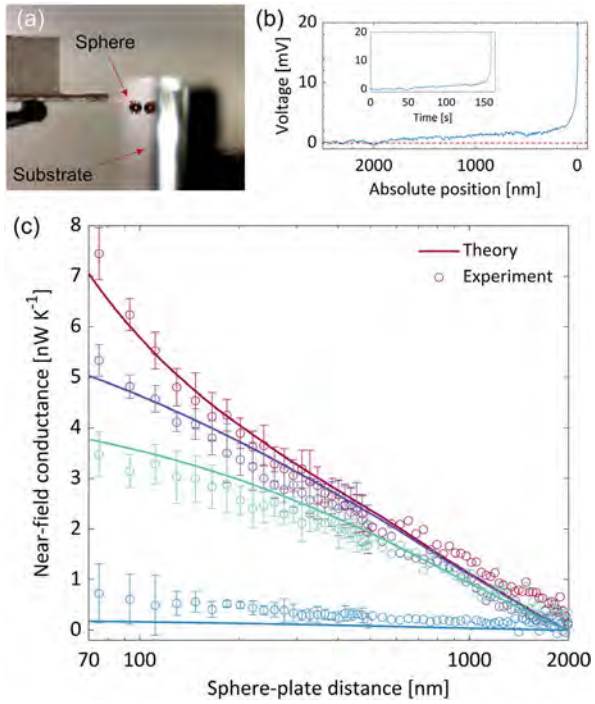

FIG. 4. Near-field experimental results. (a) Picture of the silicon substrate and the silica microsphere. A red laser shines on the bimaterial cantilever. (b) Position-dependent deflection signals converted from real-time signals acquired using the optical measurement system and shown in the inset. (c) Measured near-field conductance as a function of gap for the cases without (red) and with ∼2 nm (purple), ∼5 nm (light green) and ∼100 nm (cyan) ultrathin films, compared to nonlocal theoretical predictions obtained using the Derjaguin approximation.

for the sensitivity analysis of the local and nonlocal models when the film thickness is shifted by ±0.5 nm]. As the highest conductance is obtained in the silica-bare silicon case, the conductance decreases with increasing thickness at a given separation gap. Theoretical predictions based on the local model consistently underestimate the experimental results for the cases with ∼2- and ∼5-nm-thick TDPMs. We expect with the increasing thickness, dielectric response of thin films approaches bulk response. For ∼100-nm-thick film, the signal is buried in noise, as predicted by both models.

In addition to the quantum nanophotonics applications already reported [31–37], we propose two possible methods to make use of TDPMs in near-field based applications. First, the metallic and dielectric response over distinct frequency ranges obtained with TDPMs can be exploited for filtering near-field thermal radiation. This filtering may control the emission peak frequency to match with the band gap of the photovoltaic cells, reducing waste heat and increasing device energy conversion efficiency. Second, temperature variation may change thickness of TDPMs. Relying on temperature dependent dielectric properties, near-field thermal diodes may utilize thickness sensitivity of dielectric response from TDPMs to temperature variation for adjusting the contrast between reverse and forward biases.

In summary, we have shown that the nonlocal near-field radiative heat transfer alters thermal radiation at submicron separation sizes. Our theoretical calculations indicate that the thickness and wave vector dependent dielectric response of TDPMs modifies near-field thermal radiation between silica and doped silicon dominated by surface phonon polariton contributions. Our experiments have found that the local prediction underestimates the measured results, and verified the nonlocal near-field thermal radiation. We expect that our nonlocal consideration will change the focal point of studies about the nonlocal near-field thermal radiation from extreme near-field regions to tens and even hundreds of nanometer gap sizes. The nonlocal effect based on TDPMs provides a new degree of freedom for controlling near-field radiation, which has important implications in energy conversion and thermal management. We also foresee that material dimensions much smaller than the characteristic wavelength in both lateral and normal directions will give rise to new phenomena and applications on near-field thermal radiation.

This work was supported by the Defense Threat Reduction Agency (Grant No. HDTRA1-19-1- 0028) and the National Science Foundation (Grant No. CBET-1931964). S.-A. B. acknowledges support from the Heisenberg Programme of the Deutsche Forschungsgemeinschaft (DFG, German Research Foundation), Project No. 404073166. I. V. B. is supported by the U.S. National Science Foundation under Condensed Matter Theory Program Grant No. DMR-1830874. I. V. B. acknowledges the hospitality of the Kavli Institute for Theoretical Physics (KITP), UC Santa Barbara, during his invited visit as a KITP Fellow 2022–23 made possible by the Heising-Simons Foundation. I. V. B., S.-A. B., and S. S. gratefully acknowledge support from the KITP under U.S. National Science Foundation Grant No. PHY-1748958, where this collaborative work was started.

*sshen1@cmu.edu

[1] A. Fiorino, L. Zhu, D. Thompson, R. Mittapally, P. Reddy, and E. Meyhofer, Nanogap near-field thermophotovoltaics, Nat. Nanotechnol. **13**, 806 (2018).
[2] G. R. Bhatt, S. Zhao, Bo Roberts, I. Datta, A. Mohanty, T. Lin, J.-M. Hartmann, R. St-Gelais, S. Fan, and M. Lipson, Integrated near-field thermo-photovoltaics for heat recycling, Nat. Nanotechnol. **12**, 2545 (2020).
[3] J. Desutter, L. Tang, and M. Francoeur, A near-field radiative heat transfer device, Nat. Nanotechnol. **14**, 751 (2019).
[4] L. Zhu, A. Fiorino, D. Thompson, R. Mittapally, E. Meyhofer, and P. Reddy, Near-field photonic cooling through control of the chemical potential of photons, Nature (London) **566**, 239 (2019).
[5] A. Fiorino, D. Thompson, L. Zhu, R. Mittapally, S.-A. Biehs, O. Bezencenet, N. El-Bondry, S. Bansropun, P. Ben-Abdallah, E. Meyhofer *et al.*, A thermal diode based on nanoscale thermal radiation, ACS Nano **12**, 5774 (2018).
[6] K. Ito, K. Nishikawa, A. Miura, H. Toshiyoshi, and H. Iizuka, Dynamic modulation of radiative heat transfer beyond the blackbody limit, Nano Lett. **17**, 4347 (2017).
[7] B. Song, D. Thompson, A. Fiorino, Y. Ganjeh, P. Reddy, and E. Meyhofer, Radiative heat conductances between dielectric and metallic parallel plates with nanoscale gaps, Nat. Nanotechnol. **11**, 509 (2016).
[8] R. St-Gelais, L. Zhu, S. Fan, and M. Lipson, Near-field radiative heat transfer between parallel structures in the deep subwavelength regime, Nat. Nanotechnol. **11**, 515 (2016).
[9] E. Rousseau, A. Siria, G. Jourdan, S. Volz, F. Comin, J. Chevrier, and J.-J. Greffet, Radiative heat transfer at the nanoscale, Nat. Photonics **3**, 514 (2009).
[10] R. S. Ottens, V. Quetschke, Stacy Wise, A. A. Alemi, R. Lundock, G. Mueller, D. H. Reitze, D. B. Tanner, and B. F. Whiting, Near-Field Radiative Heat Transfer between Macroscopic Planar Surfaces, Phys. Rev. Lett. **107**, 014301 (2011).
[11] S. Shen, A. Narayanaswamy, and G. Chen, Surface phonon polaritons mediated energy transfer between nanoscale gaps, Nano Lett. **9**, 2909 (2009).
[12] H. Salihoglu and X. Xu, Near-field thermal radiation between two plates with sub-10 nm vacuum separation, Nano Lett. **20**, 6091 (2020).
[13] A. Kittel, W. Müller-Hirsch, J. Parisi, S.-A. Biehs, D. Reddig, and M. Holthaus, Near-Field Heat Transfer in a Scanning Thermal Microscope, Phys. Rev. Lett. **95**, 224301 (2005).
[14] P.-O. Chapuis, S. Volz, C. Henkel, K. Joulain, and J.-J. Greffet, Effects of spatial dispersion in near-field radiative heat transfer between two parallel metallic surfaces, Phys. Rev. B **77**, 035431 (2008).

[15] C. Henkel and K. Joulain, Electromagnetic field correlations near a surface with a nonlocal optical response, Appl. Phys. B **84**, 61 (2006).

[16] F. Singer, Y. Ezzahri, and K. Joulain, Near field radiative heat transfer between two nonlocal dielectrics, J. Quant. Spectrosc. Radiat. Transfer **154**, 55 (2015).

[17] A. I. Volokitin and B. N. J. Persson, Radiative heat transfer between nanostructures, Phys. Rev. B **63**, 205404 (2001).

[18] K. Kloppstech, N. Könne, S.-A. Biehs, A. W. Rodriguez, L. Worbes, D. Hellmann, and A. Kittel, Giant heat transfer in the crossover regime between conduction and radiation, Nat. Commun. **8**, 14475 (2017).

[19] L. Cui, V. Jeong, Wonho Fernández-Hurtado, J. Feist, F. J. García-Vidal, J. C. Cuevas, E. Meyhofer, and P. Reddy, Study of radiative heat transfer in Ångström- and nanometre-sized gaps, Nat. Commun. **8**, 14479 (2017).

[20] K. Kim, B. Song, V. Fernández-Hurtado, W. Lee, W. Jeong, L. Cui, D. Thompson, J. Feist, T. Homer Reid, F. J. García-Vidal, J. Carlos Cuevas, E. Meyhofer, and P. Reddy, Radiative heat transfer in the extreme near field, Nature (London) **528**, 387 (2015).

[21] M. Lim, J. Song, S. S. Lee, and B. J. Lee, Tailoring near-field thermal radiation between metallo-dielectric multilayers using coupled surface plasmon polaritons, Nat. Commun. **9**, 4302 (2018).

[22] D. Thompson, L. Zhu, E. Meyhofer, and P. Reddy, Nanoscale radiative thermal switching via multi-body effects, Nat. Nanotechnol. **15**, 99 (2020).

[23] K. Shi, Z. Chen, X. Xu, J. Evans, and S. He, Optimized colossal nearfield thermal radiation enabled by manipulating coupled plasmon polariton geometry, Adv. Mater. **33**, 2106097 (2021).

[24] R. A. Maniyara, D. Rodrigo, R. Yu, J. Canet-Ferrer, D. S. Ghosh, R. Yongsunthon, D. E. Baker, A. Rezikyan, F. J. García de Abajo, and V. Pruneri, Tunable plasmons in ultrathin metal films, Nat. Photonics **13**, 328 (2019).

[25] Z. M. Abd El-Fattah, V. Mkhitaryan, J. Brede, L. Fernández, C. Li, Q. Guo, A. Ghosh, A. R. Echarri, D. Naveh, F. Xia, J. E. Ortega, and F. J. García De Abajo, Plasmonics in atomically thin crystalline silver films, ACS Nano **13**, 7771 (2019).

[26] A. Boltasseva and V. M. Shalaev, Transdimensional photonics, ACS Photonics **6**, 1 (2019).

[27] D. Shah, M. Yang, Z. Kudyshev, X. Xu, V. M. Shalaev, I. V. Bondarev, and A. Boltasseva, Thickness-dependent drude plasma frequency in transdimensional plasmonic tin, Nano Lett. **22**, 4622 (2022).

[28] N. Rivera, I. Kaminer, B. Zhen, J. D. Joannopoulos, and M. Soljačić, Shrinking light to allow forbidden transitions on the atomic scale, Science **353**, 263 (2016).

[29] L. V. Keldysh, Coulomb interaction in thin semiconductor and semimetal films, Sov. Phys. JETP **29**, 658 (1979).

[30] N. S. Rytova, Screened potential of a point charge in a thin film, Moscow Univ. Phys. Bull. **3** (1967).

[31] F. H. da Jornada, L. Xian, A. Rubio, and S. G. Louie, Universal slow plasmons and giant field enhancement in atomically thin quasi-two-dimensional metals, Nat. Commun. **11**, 1 (2020).

[32] F. J. García De Abajo and A. Manjavacas, Plasmonics in atomically thin materials, Faraday Discuss. **178**, 87 (2015).

[33] H. Qian, Y. Xiao, and Z. Liu, Giant Kerr response of ultrathin gold films from quantum size effect, Nat. Commun. **7**, 13153 (2016).

[34] I. V. Bondarev, Controlling single-photon emission with ultrathin transdimensional plasmonic films, Ann. Phys. (Amsterdam) **2200331**, 1 (2022).

[35] I. V. Bondarev and C. M. Adhikari, Collective Excitations and Optical Response of Ultrathin Carbon-Nanotube Films, Phys. Rev. Appl. **15**, 034001 (2021).

[36] I. V. Bondarev, H. Mousavi, and V. M. Shalaev, Transdimensional epsilon-near-zero modes in planar plasmonic nanostructures, Phys. Rev. Res. **2**, 013070 (2020).

[37] I. V. Bondarev, H. Mousavi, and V. M. Shalaev, Optical response of finite-thickness ultrathin plasmonic films, MRS Commun. **8**, 1092 (2018).

[38] M. Francoeur, M. P. Mengüç, and R. Vaillon, Near-field radiative heat transfer enhancement via surface phonon polaritons coupling in thin films, Appl. Phys. Lett. **93**, 43109 (2008).

[39] P. Ben-Abdallah, K. Joulain, J. Drevillon, and G. Domingues, Near-field heat transfer mediated by surface wave hybridization between two films, J. Appl. Phys. **106** (2009).

[40] S. A. Biehs, Thermal heat radiation, near-field energy density and near-field radiative heat transfer of coated materials, Eur. Phys. J. B **58**, 423 (2007).

[41] See Supplemental Material at http://link.aps.org/supplemental/10.1103/PhysRevLett.131.086901 for dielectric properties, reflection and transmission coefficients, sample preparation, topography measurements, thickness sensitivity analysis, and details of experimental procedure, which includes Refs. [42–47].

[42] M. A. Ordal, R. J. Bell, R. W. Alexander, L. L. Long, and M. R. Querry, Optical properties of fourteen metals in the infrared and far infrared: Al, Co, Cu, Au, Fe, Pb, Mo, Ni, Pd, Pt, Ag, Ti, V, and W, Appl. Opt. **24**, 4493 (1985).

[43] E. D. Palik, *Handbook of Optical Constants of Solids*, Vol. 3 (Academic Press, New York, 1998).

[44] C. J. Fu, Z. M. Zhang, and G. W. Woodruff, Nanoscale radiation heat transfer for silicon at different doping levels, Int. J. Heat Mass Transfer **49**, 1703 (2006).

[45] M. Yasaka, X-ray thin-film measurement techniques v. x-ray reflectivity measurement, Rigaku J. **26** (2010).

[46] S. Shen, A. Narayanaswamy, S. Goh, and G. Chen, Thermal conductance of bimaterial microcantilevers, Appl. Phys. Lett. **92**, 063509 (2008).

[47] A. Narayanaswamy and N. Gu, Heat transfer from freely suspended bimaterial microcantilevers, J. Heat Transfer **133**, 042401 (2011).

[48] I. V. Bondarev and V. M. Shalaev, Universal features of the optical properties of ultrathin plasmonic films, Opt. Mater. Express **7**, 3731 (2017).

[49] S.-A. Biehs and I. V. Bondarev, Far- and near-field heat transfer in transdimensional plasmonic film systems, Adv. Opt. Mater. **2202712** (2023).

[50] J. Shi, B. Liu, P. Li, L. Y. Ng, and S. Shen, Near-field energy extraction with hyperbolic metamaterials, Nano Lett. **15**, 1217 (2015).

[51] J. Shi, P. Li, B. Liu, and S. Shen, Tuning near field radiation by doped silicon, Appl. Phys. Lett. **102**, 183114 (2013).

Supplemental Material

Nonlocal Near-field Radiative Heat Transfer by Transdimensional Plasmonics

Hakan Salihoglu[1], Jiawei Shi[1], Zhuo Li[1], Zexiao Wang[1], Xiao Luo[1], Igor V. Bondarev[2], Svend-Age Biehs[3], Sheng Shen[1,*]

[1] Department of Mechanical Engineering, Carnegie Mellon University, Pittsburgh, Pennsylvania 15213, USA

[2] Mathematics & Physics Department, North Carolina Central University, Durham, North Carolina 27707, USA

[3] Institut für Physik, Carl von Ossietzky Universität, 26111, Oldenburg, Germany

1. Dielectric properties of TDPM based on local and nonlocal approaches

To compute near-field thermal radiation based on the local response, we use the well-known Drude model for dielectric properties of the TDPM film, given by

$$\varepsilon(\omega) = 1 - \frac{\omega_{p,Bulk}^2}{\omega(\omega+i\gamma)}. \quad \text{(S1)}$$

Here, ω is frequency, $\gamma = 1.05 \times 10^{14}$ rad.s^{-1} is damping coefficient, $\omega_{p,Bulk} = 7.812 \times 10^{15}$ rad.s^{-1} is plasma frequency of bulk material. [1]

To compute near-field thermal radiation based on the nonlocal response, we use the nonlocal Drude dielectric response for TDPMs as given by [2,3]

$$\frac{\varepsilon(\kappa,\omega)}{\varepsilon_b} = 1 - \frac{\omega_p^2(\kappa)}{\omega(\omega+i\gamma)}, \quad \text{(S2)}$$

where ω_p is thickness dependent plasma frequency, γ is damping coefficient as given for bulk material and $\varepsilon_b = 35$ is background dielectric response of TDPM film. For our computations, we use the thickness dependent plasma frequency given by

$$\omega_p(k) = \frac{\omega_{p,Bulk}}{\sqrt{1+(\varepsilon_1+\varepsilon_2)/\varepsilon_b \kappa t}}. \quad \text{(S3)}$$

Here, $\omega_{p,Bulk}$ is plasma frequency of bulk material as given above. $\varepsilon_1 = 1$ and ε_2 are dielectric permittivity of vacuum and silicon substrate (super and substrates of the TDPM film), respectively.

2. Dielectric properties of silica and p-doped silicon

We report dielectric properties of silica and doped silicon.

To express dielectric properties of silica, we use the values reported in Ref [4].

Dielectric properties of silicon are given by the following expression,

$$\epsilon_{Si}(\omega) = \epsilon_{bl} - \frac{N_e e^2/(\epsilon_o m_e^*)}{\omega^2+i\omega/\tau_e} - \frac{N_h e^2/(\epsilon_o m_h^*)}{\omega^2+i\omega/\tau_h}, \quad \text{(S4)}$$

where ω is radial frequency, ϵ_{bl} is dielectric function of intrinsic silicon, N_x is carrier concentration of electrons, ($x = e$), and holes, ($x = h$), m_i^* is effective mass, and τ_i is scattering time, ϵ_o is vacuum permittivity , e is elementary charge. ϵ_{bl} is given by $(n_{bl} - i\kappa_{bl})^2$ where n_{bl} stands for refractive index, κ_{bl} denotes the extinction coefficient of intrinsic silicon, and i is unit imaginary number. For the frequency range of interest, n_{bl}~3.42, [4] and κ_{bl} is taken from Ref [4]. For silicon used in our experiment, $N_h = 3.09 \times 10^{19}$ cm-3, and N_e is found using N_{th}^2/N_h where $N_{th}^2 = N_C N_V \exp(-E_g/k_B T)$. $N_C (= 2.86 \times 10^{19}$ cm^{-3} at 300 K) and $N_V (= 2.66 \times 10^{19}$ cm^{-3} at 300 K) are the effective densities of states in conduction and valence bands, respectively. [5] Here, E_g is band gap energy and depends on temperature, T, with $E_g = 1.17 - 0.000437T^2/(T + 636)$. $m_e^* = 0.27m_o$ and $m_h^* = 0.37m_o$ where m_o is free electron mass. $\tau_{e,h}$ is found from $\tau_{e,h} = m_{e,h}^* \mu/e$ where mobility, μ, is determined using Hall effect measurements as reported in Ref [6].

3. Imaginary components of dielectric responses based on the local and nonlocal models

In the main text, we report the real component of dielectric responses. Here, results for the imaginary components of the corresponding conditions are given.

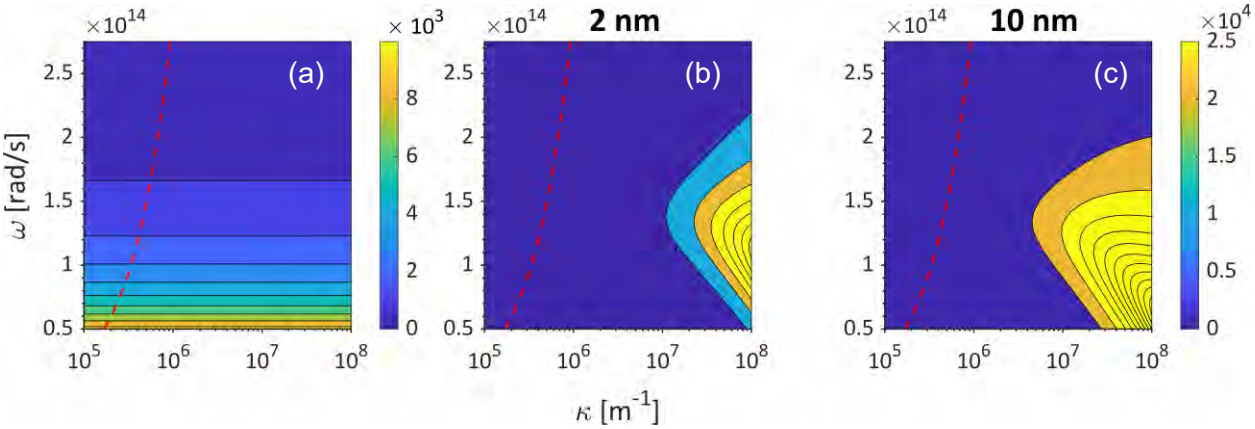

FIG. S1. Imaginary component of dielectric responses based on the local and nonlocal approaches. Local (a) response is for bulk material and nonlocal (b)-(c) response is for t=2 and 10 nm. Red dashed lines represent light line, $\kappa = k_o$.

4. Fresnel reflection coefficients

Here, we report equations of Fresnel reflection coefficients and demonstrate Fresnel reflection coefficients of an assembled multilayer structure consisting of p-doped silicon with an atomically thin Pt layer for various thicknesses based on the local and nonlocal models.

To demonstrate reflection coefficients of each interface in an assembled structure, i.e. p-doped silicon and thin Pt layer, we refer to Fig. S2.

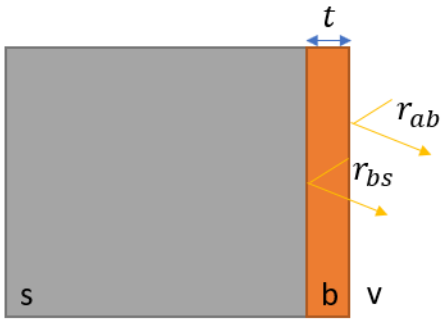

FIG. S2. Illustration of the assembly and Fresnel reflection coefficients at interfaces. The assembly consists of a plane substrate, s, a thin layer of metal, b, and vacuum, v. Thickness of the thin layer is denoted by t. r_{mn} represents the Fresnel reflection coefficient for the left-going waves from an interface sandwiched between media, m and n.

To calculate the Fresnel reflection coefficient of a multilayer(assembled) planar structure i (=1,2), we compute

$$r_i = \frac{r_{vb} + r_{bs} e^{i2k_{z,b}t}}{1 + r_{vb} r_{bs} e^{i2k_{z,b}t}} \tag{S5}$$

where r_{mn} stands for the Fresnel reflection coefficient at an interface sandwiched between materials, m and n, for the left-going waves. We note that Eq. S5 reduces to the single interface reflection when t=0. Eq. S5 is calculated for both s- and p-polarized waves. $r_{mn,s}$ and $r_{mn,p}$, where s and p represent polarizations, are given as

$$r_{mn,s} = \frac{k_{z,m} - k_{z,n}}{k_{z,m} + k_{z,n}} \tag{S6}$$

$$r_{mn,p} = \frac{\varepsilon_n k_m - \varepsilon_m k_n}{\varepsilon_n k_m + \varepsilon_m k_n} \tag{S7}$$

where m,n = b,s,v. Here, $k_m = \sqrt{\varepsilon_m \frac{\omega^2}{c^2} - \kappa^2}$ is dispersion relation of waves in material m. ε_m denotes complex dielectric function of material m (ε_v = 1 for vacuum).

To better understand the observed trends in transmission probabilities as discussed in the main text, we plot Fresnel reflection coefficients using Eq. S5 for bare p-doped silicon and p-doped silicon with a thin Pt layer of 2 and 10 nm for p-polarized propagating and evanescent waves in Figs. S3 and S4, respectively.

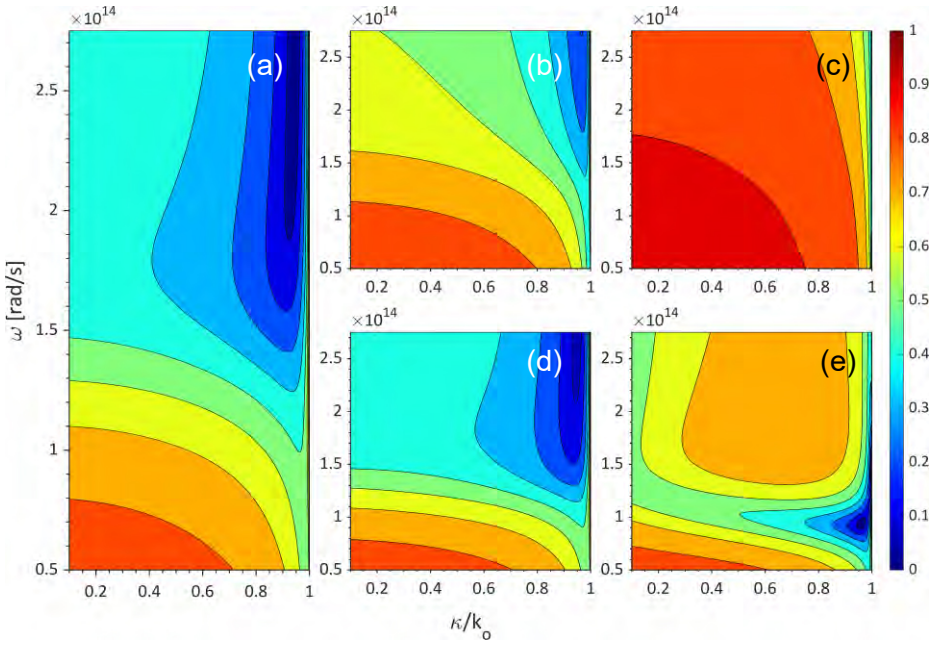

FIG. S3. Absolute value of Fresnel reflection coefficients from the p-doped silicon substrate for p-polarized propagating waves. (a) $|r_2|$ for bare silicon. (b)-(e) Top (b)-(c) and bottom (d)-(e) panels show $|r_2|$ of 2 and 10-nm thick Pt TPM based on local and nonlocal models, respectively.

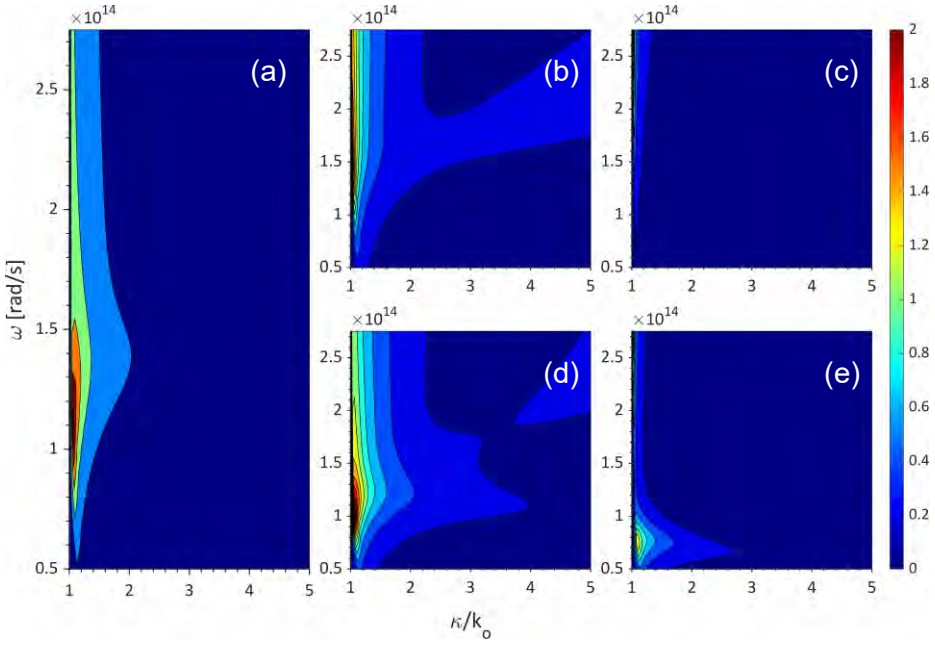

FIG. S4. Imaginary component of Fresnel reflection coefficients from the p-doped silicon substrate for p-polarized evanescent waves. (a) $Im(r_2)$ for bare silicon. (b)-(e) Top (b)-(c) and bottom (d)-(e) panels show $Im(r_2)$ of 2 and 10-nm thick Pt TPM based on local and nonlocal models, respectively.

For the completeness and the interpretation of s-polarized transmission probability given in the next section, we also include reflection coefficient results of the p-doped substrate with a thin Pt layer for s-polarized waves.

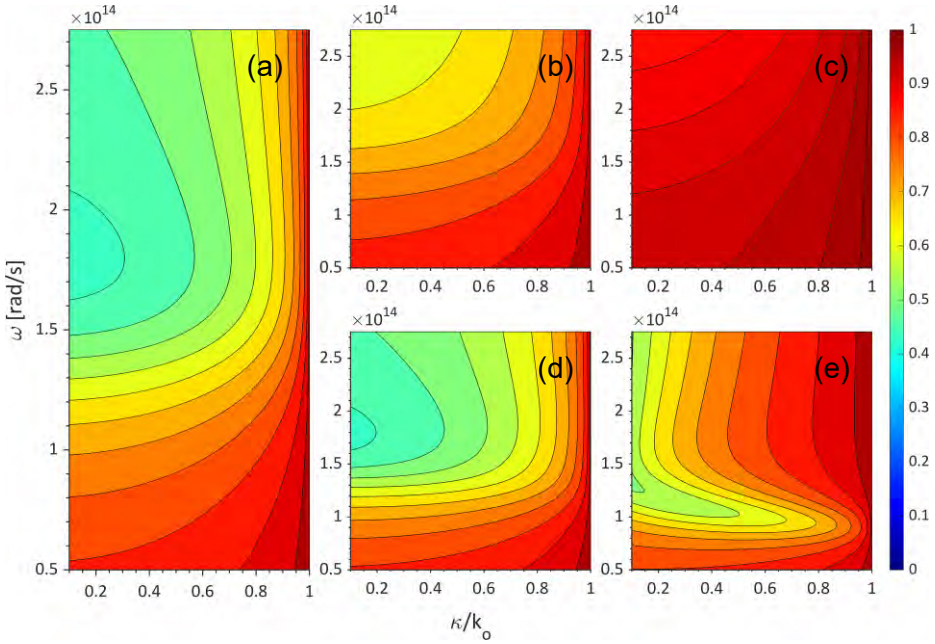

FIG. S5. Absolute value of Fresnel reflection coefficients from the p-doped silicon substrate for s-polarized propagating waves. (a) $|r_2|$ bare silicon. (b)-(e) Top (b)-(c) and bottom (d)-(e) panels show $|r_2|$ of 2 and 10-nm thick Pt TPM based on the local and nonlocal models, respectively.

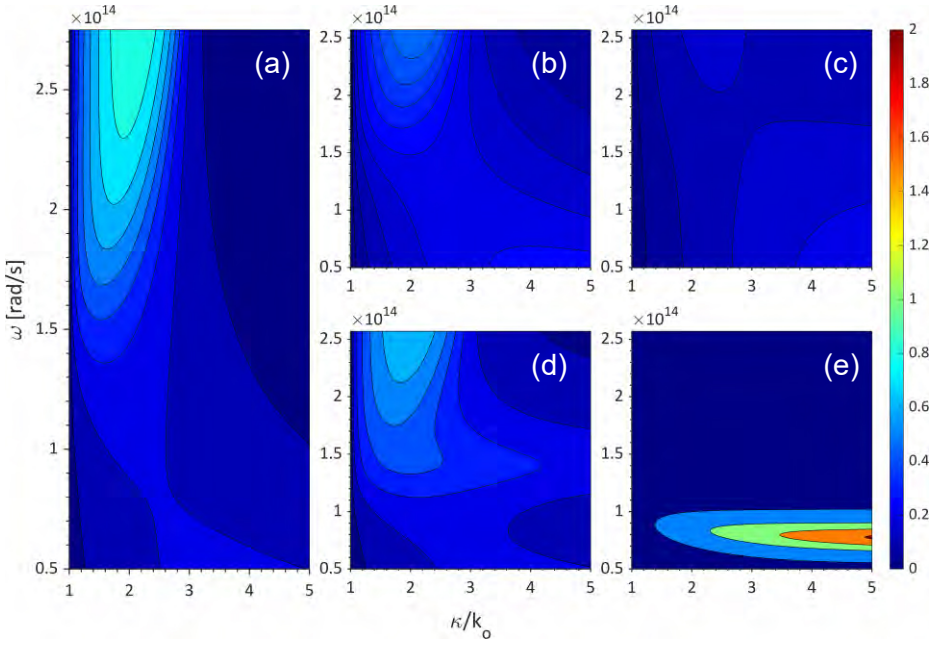

FIG. S6. Imaginary component of Fresnel reflection coefficients from the p-doped silicon substrate for s-polarized evanescent waves. (a) $Im(r_2)$ bare silicon. (b)-(e) Top (b)-(c) and bottom (d)-(e) panels show $Im(r_2)$ of 2 and 10-nm thick Pt TPM based on the local and nonlocal models, respectively.

5. Transmission coefficients

To compute the heat flux between structures i ($= 1$ for semi-infinite silica plate, and $= 2$ for multilayer planar system, semi-infinite silicon substrate with an atomically thin metal film), we need to find transmission probability, $\mathcal{T}(\omega, \kappa)$, in Eq. (1) and reflection coefficients, r_1 and r_2, in equation (2) in the main text.

Transmission probability for evanescent waves ($\kappa > k_o$) is already given in Eq. (2) in the main text. For propagating waves ($\kappa < k_o$), $\mathcal{T}(\omega, \kappa)$ takes the following form:

$$\mathcal{T}(\omega, \kappa) = \frac{(1-|r_1|^2)(1-|r_2|^2)}{|1-r_1 r_2 e^{2ik_z d}|^2}, \tag{S8}$$

$(1 - |r_i|^2)$ represents absorption (emission based on Kirchoff's law) by planar structure i. Explicit forms of the reflection coefficients are given in Section 4 of Supplemental Material. For the sake of clarity, we omit polarization dependence of $\mathcal{T}(\omega, \kappa)$ in the main text.

For the completeness, in addition to transmission probabilities of p-polarized waves given in the main text, we, here, report the probabilities of s-polarized waves for the corresponding conditions.

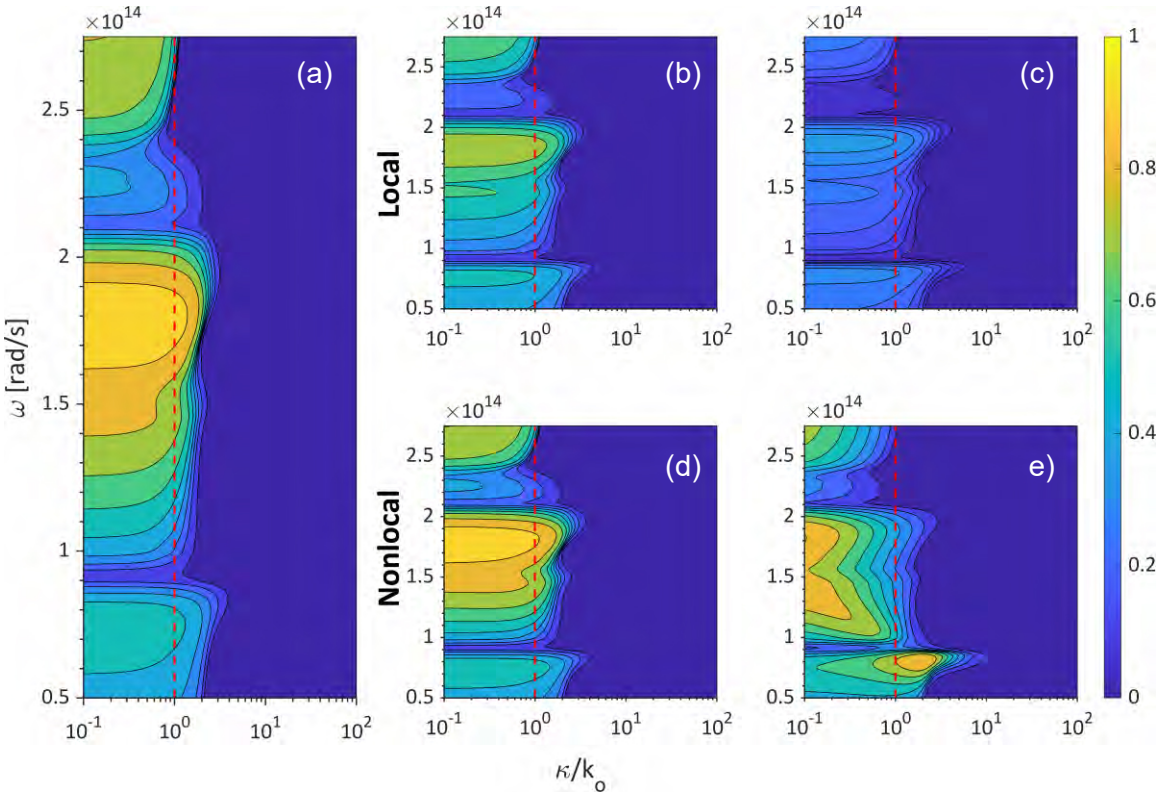

FIG. S7. Transmission probability of s-polarized waves. (a) Transmission probability across a 100-nm separation between silica and bare p-doped silicon. (b)-(c) Silica and p-doped silicon with a thin Pt layer of t=2 (b) and 10 (c) nm modelled with local responses. (d)-(e) Silica and p-doped silicon with a thin Pt layer of t=2 (d) and 10 (e) nm modelled with nonlocal responses.

6. Sample preparation

Commercially available boron doped silicon wafer with a hole concentration of $\sim 3.1 \times 10^{19}$ cm^{-3} was coated with a thin film of Pt using the sputtering technique. By controlling the plasma power, the deposition rate can be tuned as low as ~1 Å.s^{-1}. Before sputtering, buffered oxide etching was applied to remove the ~1 nm thick oxide layer. The film thicknesses were confirmed and measured using thin-film X-ray reflection (XRR) measurement technique. [7]

7. Topography obtained with Atomic Force Microscopy (AFM)

Here, we report topography measurements over 1×1-μm^2 areas used to determine the roughness of the bare silicon and the thin film surfaces used in the experiments. Figure S8 demonstrates results of 2D height profiles of (a) bare silicon substrate, silicon substrate with (a) ~2-, (b) ~5- and (c) ~100-nm thick Pt layers. The measured RMS values for bare, ~2-and ~5-nm thick layers are 0.1, 0.2 and 0.4 nm, respectively. Also, peak-to-peak roughness of the surfaces is negligibly small compared to the separation gaps measured. These results show that the film roughness is negligibly small as compared to the measured separation gaps. In addition, we performed an analysis for sensitivity of the theoretical heat conductance to thickness

variations by considering the RMS values of the roughness, as shown in Section 10 of the Supplemental Material.

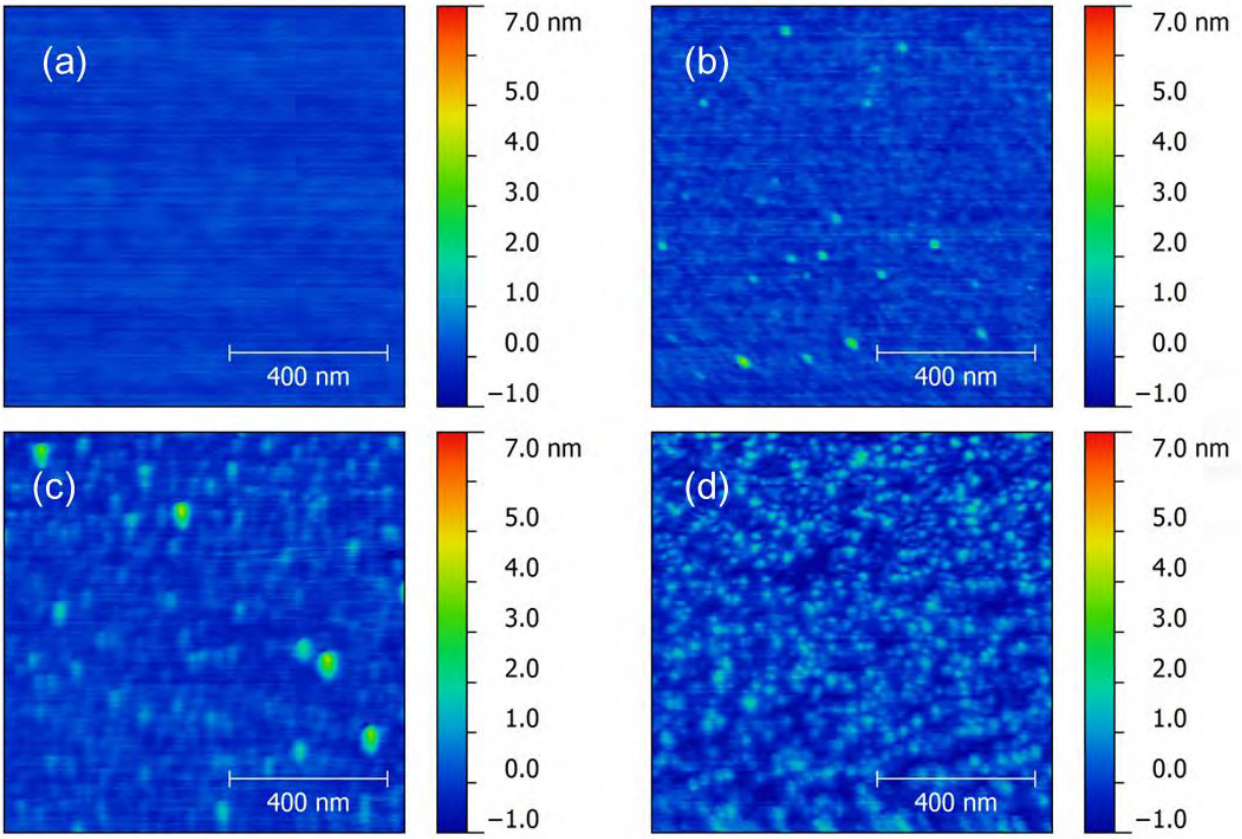

FIG. S8. Topography measurement results obtained with AFM. Roughness of center areas of surfaces for p-doped silicon without a coating (a), with a Pt layer coating of 2- (b), 5- (c) and 100- (d) nm thickness over 1 x 1 μm^2.

8. Derjaguin Approximation

To compute the near-field conductance between a sphere with radius R (50 μm in our study) and the multilayer plate system (substrate and TDPM), we exploit the Derjaguin approximation using the solutions to two parallel plates. Based on the approximation, the sphere is discretized into finite plane surfaces positioned at ($\underline{d}$,r) on the sphere surface where $\underline{d}$ is the distance between an individual finite surface and the multilayer plate system, and r is the lateral distance from the vertical axis through the center of the sphere. Accordingly, the near-field conductance, G_{NF}, for the sphere-plate configuration reads

$$G_{NF}(T,d) = \int_0^R h\left(T,\underline{d}(r)\right) 2\pi r\, dr = \int_0^R h\left(T, d + R - \sqrt{R^2 - r^2}\right) 2\pi r\, dr, \quad \text{(S12)}$$

where d is the smallest separation gap between the sphere and the multilayer plate system. h is the heat transfer coefficient for two parallel plates with a separation gap of $\underline{d}$. h is calculated by $h \sim q\left(\underline{d}\right)/\Delta T$ using

Eq. (1) and plotted for two parallel plates in Fig. 3. In all calculations, the temperature is assumed to be T ~300 K.

9. Comparison of experimental heat conductance results with local theoretical predictions

In the main text, we compare experimental results with nonlocal theoretical predictions. Here, we also present the comparison with local theoretical predictions.

Figures S9a and S9b show the comparison of experimental results with the nonlocal and local predictions, respectively. Figure S9a is the same as Fig. 4c and included for direct comparison to Fig. S9b. Figure S9b demonstrates that local theoretical predictions underestimate the experimental results for 2- and 5-nm thick Pt layers.

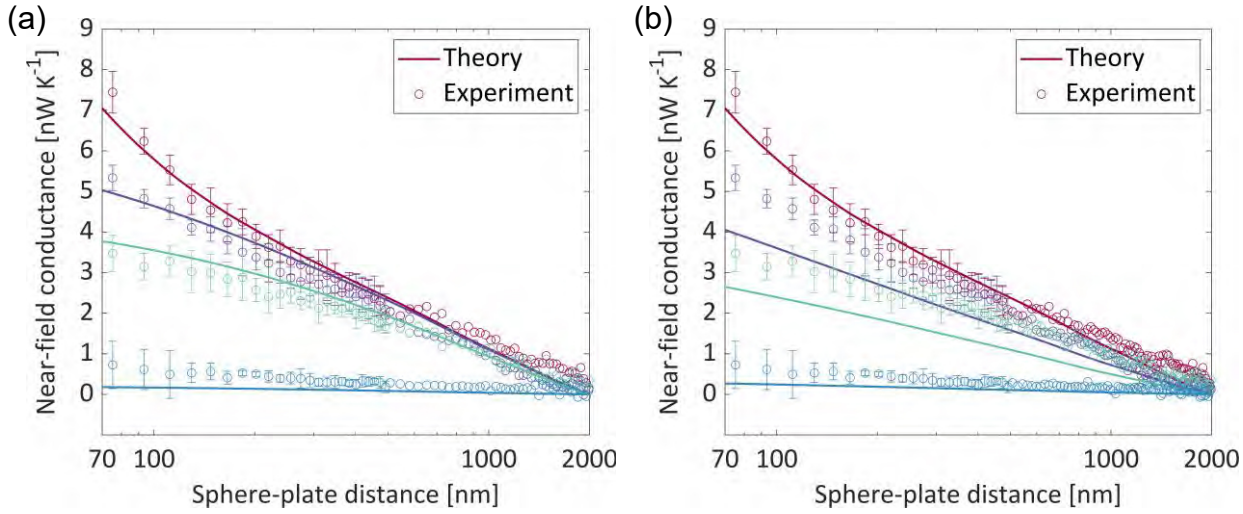

FIG. S9. Comparison of experimental results to theoretical predictions based on the local and nonlocal models. (a) Comparison of experimental results to nonlocal theoretical predictions. (b) Comparison of experimental results to local theoretical predictions. In (a) and (b), red, purple, light green, and cyan curves represent the results for silicion without a coating and with 2-, 5- and 100-nm coatings, respectively.

10. Thickness sensitivity of the local and nonlocal near-field heat conductances

We conducted sensitivity analysis to see the thickness dependence of our computations for the near-field heat conductance. The analysis is conducted only for ~2-nm and ~5-nm cases. For both cases, the RMS-roughness values reported in Section 7 of Supplemental Material are less than 0.5 nm. For the computations, we shifted thickness by ±0.5 nm from the measured thickness values using the XRR technique. Figures S10a and S10b show the sensitivity of the local and nonlocal models to thickness variation for ~2-nm and ~5-nm cases, respectively. Shaded areas in both figures represent the sensitivity regions of the corresponding predictions. We also included experimental results to clearly show the sensitivity region of the local model mismatches with the experimental results. At no separation gaps considered, the local and nonlocal estimations within the thickness variations overlap or cross.

Additionally, the sensitivity of our predictions remains significantly less than error bars of the experimental results over majority of the separation gaps.

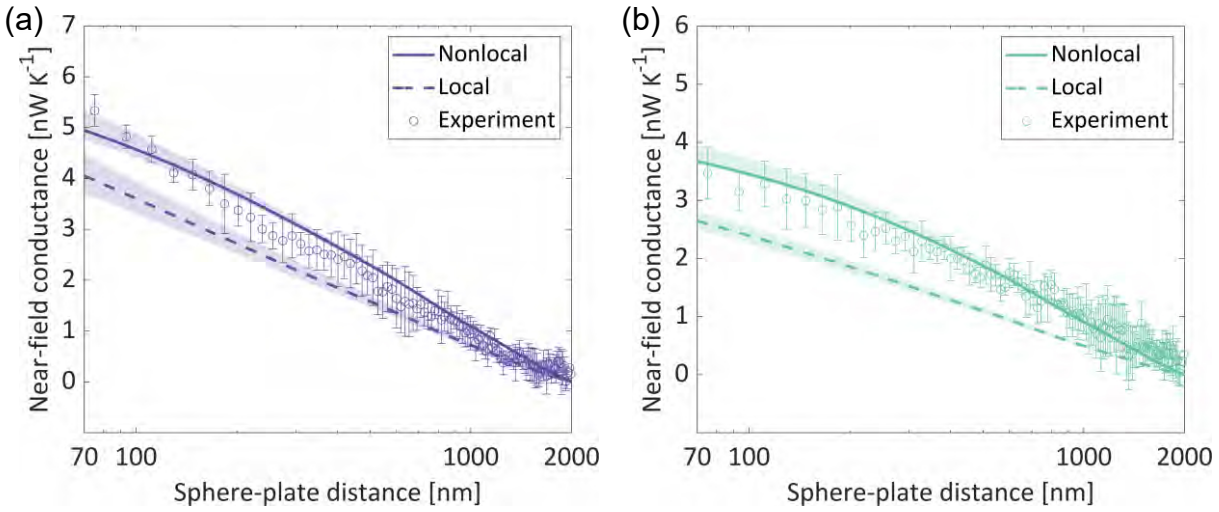

FIG. S10. Thickness sensitivity of the local and nonlocal near-field heat conductances. Comparison of the local and nonlocal predictions for the ~2-nm film (a) and for the ~5-nm film (b). The theoretical values for the 2-nm and 5-nm films. Shaded areas in both figures represent the sensitivity regions of the corresponding predictions by a ±0.5-nm thickness variation. Experimental results are included for comparison.

11. Conversion of deflection data to conductance

In our experiment, deflection signals from the detectors are converted to near-field thermal conductance. This method relies on the beam approximation of cantilevers. Details of the beam theory are given in Section 12 of Supplemental Material. To find experimental near-field conductance, G_{NF}, reported in Fig. 4c, the temperature difference between the sphere and the substrate is needed. We assume that the substrate temperature is same with the base temperature, and the absorbed power, P, generates temperature difference, ΔT, between the sphere and the base via $P = AP_{in} = G_{can}\Delta T$. Since $G_{NF} = \frac{\Delta P_{NF}}{\Delta T}$ and $\Delta P_{NF} = -R_{p-x}\Delta z$, the measured G_{NF} is $\frac{G_{can}R_{p-x}\Delta z}{AP_{in}}$. Here, R_{p-x} and G_{can} are found with calibration in the far-field as explained in Section 12 of Supplemental Material. Δz is proportional to the experimental deflection signal, P_{in} is laser power incident to the cantilever and *A* is absorptivity of the layer on the side of the cantilever facing to the laser. Note that the laser focal size is ~30 μm and the beam length, thickness and width are 200, 0.5 and 40 μm, respectively.

12. Beam Theory

Here, we explain details of the beam theory.

Any axial temperature gradient in the bi-material cantilever results in temperature induced deflection. Based on beam theory, the relation between the cantilever deflection and the temperature distribution is governed by [8]

$$\frac{d^2z}{dx^2} = 6(\alpha_a - \alpha_b)\frac{t_a+t_b}{t_a t_b K}(T(x) - T_o). \quad \text{(S10)}$$

Here, $z(x)$ denotes the deflection at the location x of the cantilever, where x measures the distance from the tip of the cantilever. α_i stands for thermal expansion coefficient of material i constituting the cantilever, and t_i is thickness of the corresponding material. T_o is neutral temperature of the cantilever and $T(x)$ is temperature along the cantilever. K is a constant depending on the bi-material of the cantilever and calculation of the constant is given in Ref [9]. To solve the beam equation for $z(x)$, the used boundary conditions at the base of the cantilever: $z|_{x=l} = 0$, and $\frac{dz}{dx}|_{x=l} = 0$, with l representing the length of the cantilever. The temperature profile in steady state for an input power, P, is found by solving a 1D steady state heat conduction equation as

$$T(x) - T_o = \left(1 - \frac{x}{l}\right)\frac{P}{G_{can}}, \quad \text{(S11)}$$

where G_{can} stands for thermal conductance of the cantilever. *P* is idealized to be a point source located at $x = 0$. Then, with the temperature profile, we can get the boundary condition of the cantilever deflection with respect to position at the tip as

$$\frac{dz}{dx}|_{x=0} = \varphi = -\frac{3lPH}{G_{can}}, \quad \text{(S12)}$$

where H is a constant determined by cantilever properties and given as $(\alpha_a - \alpha_b)(t_a + t_b)/t_a t_b K$. [9] Using this equation and following the derivation in Ref [9], we find a relation

$$\frac{\delta\varphi/\delta T_o}{\delta\varphi/\delta P} = \frac{\varphi_{T_o}}{\varphi_P} = 2G_{can}. \quad \text{(S13)}$$

φ is the slope of the cantilever deflection, dz/dx, the quantity measured in conventional AFM experiment. φ_{T_o} is found by measuring the base temperature with a K-type thermocouple at the closest location to the base after varying T_o using an external heater. φ_P is found by measuring the change in deflection signal with respect to power input. With this procedure, G_{can} is calibrated as ~0.0234 mW.K^{-1}.

The absorbed portion of the incident laser power is P, and $P = P_{can} + P_{NF}$. In near-field regime, any change in the separation gap induces changes in P_{NF}, ΔP_{NF}. Since P is constant for the near-field conductance measurement, $\Delta P_{NF} = -\Delta P_{can}$. Here, ΔP_{can} is linearly dependent to the signal, Δz, measured by the position sensing detector (PSD) through $\Delta P_{can} = R_{p-x}\Delta z$. To find R_{p-x}, a calibration process is performed in the far-field. For the calibration, we vary incident laser power P_{in}, ΔP_{in}, and measure ΔP_{ref}. Then, ΔP_{can} is derived as $\Delta P_{can} = \Delta P = A\Delta P_{in} = \frac{A}{1-A}\Delta P_{ref}$. Here, *A* represents absorptivity of top layer of the cantilever at the wavelength of incident laser light, which is 0.21 for gold

in our case. By equaling $R_{p-x}\Delta z = \frac{A}{1-A}\Delta P_{ref}$, we find $R_{p-x} = \frac{A}{1-A}\frac{\Delta P_{ref}}{\Delta z}$. As a result of the calibration at the far-field, we found R_{p-x} as 0.0507. Then, for the near-field thermal conductance measurement, G_{NF}, we can write $\Delta P_{NF} = -R_{p-x}\Delta z$. G_{NF} is related with ΔP_{NF} via $G_{NF} = \Delta P_{NF}/\Delta T$. Therefore, to find the measured near-field thermal conductance from the measured signal, Δz, we use the relation, $G_{NF} = \frac{G_{can}R_{p-x}\Delta z}{AP_{in}}$.

References:

[1] M. A. Ordal, R. J. Bell, R. W. Alexander, L. L. Long, and M. R. Querry, *Optical Properties of Fourteen Metals in the Infrared and Far Infrared: Al, Co, Cu, Au, Fe, Pb, Mo, Ni, Pd, Pt, Ag, Ti, V, and W*, Appl. Opt. **24**, 4493 (1985).

[2] I. V. Bondarev and V. M. Shalaev, *Universal Features of the Optical Properties of Ultrathin Plasmonic Films*, Opt. Mater. Express **7**, 3731 (2017).

[3] D. Shah, M. Yang, Z. Kudyshev, X. Xu, V. M. Shalaev, I. V. Bondarev, and A. Boltasseva, *Thickness-Dependent Drude Plasma Frequency in Transdimensional Plasmonic TiN*, Nano Lett. **22**, 4622 (2022).

[4] E. D. Palik, *Handbook of Optical Constants of Solids* (Academic Press, 1998).

[5] C. J. Fu, Z. M. Zhang, and G. W. Woodruff, *Nanoscale Radiation Heat Transfer for Silicon at Different Doping Levels*, (2005).

[6] J. Shi, P. Li, B. Liu, and S. Shen, *Tuning near Field Radiation by Doped Silicon*, Appl. Phys. Lett. **102**, (2013).

[7] M. Yasaka, *X-Ray Thin-Film Measurement Techniques V. X-Ray Reflectivity Measurement*, Rigaku J. **26**, (2010).

[8] S. Shen, A. Narayanaswamy, S. Goh, and G. Chen, *Thermal Conductance of Bimaterial Microcantilevers*, Appl. Phys. Lett. **92**, (2008).

[9] A. Narayanaswamy and N. Gu, *Heat Transfer from Freely Suspended Bimaterial Microcantilevers*, J. Heat Transfer **133**, 1 (2011).